Nano-Micro Letters

e-ISSN 2150-5551
CN 31-2103/TB

ARTICLE

https://doi.org/10.1007/s40820-023-01221-3

Cite as
Nano-Micro Lett.
(2024) 16:5

Received: 28 June 2023
Accepted: 24 September 2023

Understanding Bridging Sites and Accelerating Quantum Efficiency for Photocatalytic CO_2 Reduction

Kangwang Wang[1], Zhuofeng Hu[2], Peifeng Yu[1], Alina M. Balu[3], Kuan Li[1], Longfu Li[1], Lingyong Zeng[1], Chao Zhang[1], Rafael Luque[4,5], Kai Yan[2] ✉, Huixia Luo[1] ✉

HIGHLIGHTS

- The S-vacancies result in the change of d-band electronic state of Mo.
- An internal quantum efficiency of 94.01% at 380 nm for photocatalytic CO_2 reduction reaction (CO_2RR).
- The Mo–S bridging bonds optimize adsorption energies and accelerate CO_2RR kinetics.

ABSTRACT We report a novel double-shelled nanoboxes photocatalyst architecture with tailored interfaces that accelerate quantum efficiency for photocatalytic CO_2 reduction reaction (CO_2RR) via Mo–S bridging bonds sites in S_v–In_2S_3@2H–$MoTe_2$. The X-ray absorption near-edge structure shows that the formation of S_v–In_2S_3@2H–$MoTe_2$ adjusts the coordination environment via interface engineering and forms Mo–S polarized sites at the interface. The interfacial dynamics and catalytic behavior are clearly revealed by ultrafast femtosecond transient absorption, time-resolved, and in situ diffuse reflectance–Infrared Fourier transform spectroscopy. A tunable electronic structure through steric interaction of Mo–S bridging bonds induces a 1.7-fold enhancement in S_v–In_2S_3@2H–$MoTe_2$(5) photogenerated carrier concentration relative to pristine S_v–In_2S_3. Benefiting from lower carrier transport activation energy, an internal quantum efficiency of 94.01% at 380 nm was used for photocatalytic CO_2RR. This study proposes a new strategy to design photocatalyst through bridging sites to adjust the selectivity of photocatalytic CO_2RR.

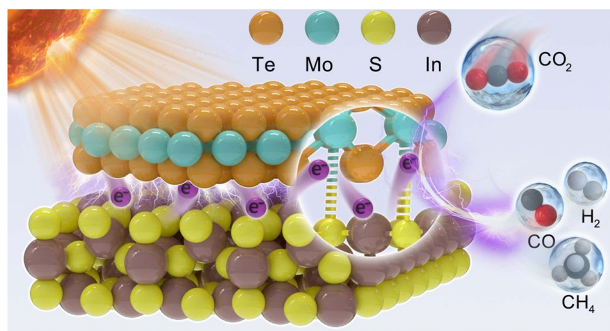

KEYWORDS Quantum efficiency; Electronic structure; Steric interaction; Bridging sites; CO_2 reduction

✉ Kai Yan, yank9@mail.sysu.edu.cn; Huixia Luo, luohx7@mail.sysu.edu.cn
[1] School of Materials Science and Engineering, State Key Laboratory of Optoelectronic Materials and Technologies, Guangdong Provincial Key Laboratory of Magnetoelectric Physics and Devices, Key Lab of Polymer Composite and Functional Materials, Sun Yat-Sen University, No. 135, Xingang Xi Road, Guangzhou 510275, People's Republic of China
[2] School of Environmental Science and Engineering, Sun Yat-Sen University, No. 135, Xingang Xi Road, Guangzhou 510275, People's Republic of China
[3] Departamento de Química Orgánica, Universidad de Córdoba, Campus Universitario de Rabanales, Edificio Marie Curie (C3), 14014 Córdoba, Spain
[4] Center for Refining and Advanced Chemicals, King Fahd University of Petroleum and Minerals, 31261 Dhahran, Saudi Arabia
[5] Universidad ECOTEC, Km 13.5 Samborondón, EC092302 Samborondón, Ecuador

Published online: 06 November 2023

1 Introduction

Two of the largest research challenges confronting the world today are the ever-rising need for clean energy and the global crisis of climate change [1]. Converting solar energy by means of the mild light-driven chemical reactions is of far-reaching importance for the development of green and sustainable energy sources [2]. A wide variety of exciting products resulting from carbon dioxide (CO_2) conversion are CH_3OH, CH_4, and other available organic compounds, which are stable, nontoxic substances with considerable market potential in various applications [3, 4]. Unfortunately, CO_2 reduction reaction (CO_2RR) frequently is difficult to carry out owing to CO_2 being thermodynamically stable, resulting in extraordinarily andante reaction kinetics during the photoreduction process. Beyond that, the conversion of CO_2 molecules competes with other side reactions, such as the common hydrogen (H_2) evolution reaction (HER, $2H^+ + 2e = H_2$), which memorably declines the production of reduced carbon products. For this reason, highly selective, stable and efficient catalysts are required to facilitate photocatalytic CO_2RR, overcoming significant energy barriers and tuning the reaction pathways to the formation of CH_3OH and CH_4, as well CO [5].

Two-dimensional (2D) materials, especially transition metal dichalcogenides (TMDs, MX_2) [M refers to a transition metal (Ta, Nb, Mo, and W, etc.), and X denotes as a chalcogen (S, Se, and Te, etc.)] have been extensively studied and applied in many fields for decades, because of their low cost, superior electronic, topological and mechanical properties, as well as their ultrathin low-dimensional nature. By now, the members of TMDs group, on account of their unique electronic and atomic structural behavior, have been widely considered to be an ideal alternative for photocatalytic and electrocatalytic CO_2RR. Despite the emergence of many fascinating preponderances, inadequate intrinsic electrical transport and inactive substrate surfaces in the TMDs group severely impede their application in photocatalytic and electrocatalytic CO_2RR, for instance, typical molybdenum sulfide (MoS_2) and molybdenum selenide ($MoSe_2$) materials [6]. It is interesting to notice that molybdenum telluride ($MoTe_2$) has recently attracted attention due to its metallic conductivity and outstanding electron transport capacity. The existence of different phases of $MoTe_2$ provides the feasibility of developing a wealth of novel structures and gadgets, including a semiconducting 2H-phase (prismatic trigonal structure; bandgap of about 1.0 eV), a topological semimetallic 1 T-phase (twisted octahedron; energy gap covered near the Fermi energy level (E_F)), and a possible topological superconducting T_d-phase, which facilitates the commercial application of $MoTe_2$ in the physical industry [7, 8]. Despite this, the construction of catalytically active nano-heterojunctions with novel compositions and microscopic morphologies remains a major challenge requiring urgent breakthroughs due to the challenges of synthetic methods and design ideas.

Based on previously reported studies, designing double-shelled hollow structures of semiconductor nanomaterials is one of the most effective stratagems to for improving light utilization, tuning electronic structure and steric interaction of chemical bonds, accelerating interfacial contact, providing more catalytic reaction sites and promoting effective carrier separation and transfer. Given this, we strategically proposed a "double-shelled nanoboxes" design for S_v–In_2S_3@2H–$MoTe_2$ catalysts, in which 2H–$MoTe_2$ was coated on S_v–In_2S_3 single-shelled nanoboxes to form the Mo–S bonds of S-vacancies-rich junction structure. Assisted by the robust built–In electric field (IEF) and Mo–S bridging bonds of S_v–In_2S_3@2H–$MoTe_2$(5), "S"-scheme charge separation is notably facilitated, resulting in an internal quantum efficiency (IQE) calculated via photocatalytic CO_2RR of 94.01% (IQE_{cr}) at 380 nm. Particularly, the Mo–S bridging bonds can reduce the adsorption energy barriers of *OCHO and *CHO species and effectively regulate the formation energy barriers of CO, H_2, and CH_4, thus enhancing the photocatalytic activity (Scheme 1).

2 Experimental Section

2.1 Materials

Indium chloride ($InCl_3$) and sodium hydroxide (NaOH) were purchased from Sinopharm Group Chemical Reagent Co., Ltd. Copper sulfate ($CuSO_4$•$5H_2O$) was purchased from Acros Organics with a purity of over 99.99%. Tellurium powder (Te, more than 200 mesh) was purchased from Shanghai Aladdin Biochemical Technology Co.,

 https://doi.org/10.1007/s40820-023-01221-3

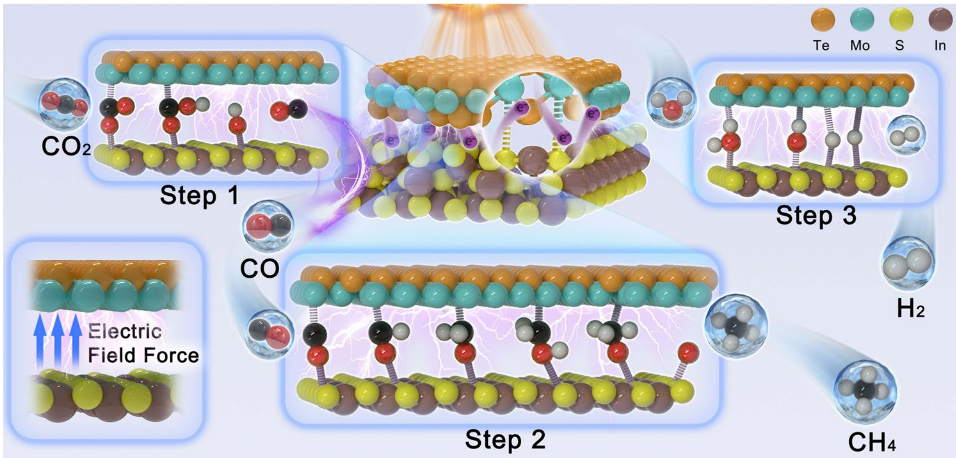

Scheme 1 Schematic illustration for modulating Mo–S bonds coupling step in CO_2 reduction pathways over S_v–In_2S_3@2H–$MoTe_2$(5)

Ltd. Hydrazine hydrate ($N_2H_4·H_2O$) was purchased from Sinopharm Group Chemical Reagent Co., Ltd. Sodium molybdate ($Na_2MoO_4·2H_2O$) was supplied by Aladdin Reagent Co., Ltd. (Shanghai, China). Polyvinylpyrrolidone (PVP, Mw = 400,000) was provided by Shanghai Ryon Biotechnology Co., Ltd. (Shanghai, China). Sodium thiosulfate ($Na_2S_2O_3$), with a purity of over 99.5%, was purchased from Shanghai Aladdin Biochemical Technology Co., Ltd. (Shanghai, China). Dimethyl sulfoxide (DMSO) and thioacetamide (C_2H_5NS) were purchased from Sigma with a purity of over 99.99%. All of the reagents used in our experiments were analytical purity and used without further purification.

2.2 Preparation of In_2S_3, S_v–In_2S_3, 2H–$MoTe_2$ and S_v–In_2S_3@2H–$MoTe_2$

2.2.1 Preparations of the In_2S_3 SSNBs

The as-prepared $In(OH)_3$ single-shelled nanoboxes (SSNBs) and 40 mg of C_2H_5NS were dispersed into 20 mL of ethanol. The solution was transferred into a Teflon-lined stainless autoclave and heated at 90 °C in an oven for 2 h. The precipitate was harvested by centrifugation, washed with DW and ethanol several times, and subsequently annealed in N_2 at 300 °C for 2 h to obtain the In_2S_3 SSNBs.

2.2.2 Preparations of the S_v–In_2S_3 SSNBs

S-vacancies-rich In_2S_3 SSNBs (S_v–In_2S_3 SSNBs) were prepared via an $N_2H_4·H_2O$-assisted hydrothermal method. Typically, the as-synthesized In_2S_3 SSNBs (100 mg) were dispersed into 20 mL of deionized water for 1 h, and 5 mL $N_2H_4·H_2O$ was added into the mixing solution and stirred for another 30 min. Afterward, the mixture was transferred to a 50 mL autoclave and maintained at a 240 °C oven for 5 h. Finally, the precipitate was separated by centrifugation, washed with DW and ethanol several times, then dried at 60 °C for 10 h.

2.2.3 S_v–In_2S_3@2H–$MoTe_2$ Double-Shelled Nanoboxes (DSNBs)

The S_v–In_2S_3@2H–$MoTe_2$ DSNBs were synthesized by a similar process to S_v–In_2S_3 SSNBs, except that $Na_2MoO_4·2H_2O$ and Te powders were added to the mixture. The S_v–In_2S_3@2H–$MoTe_2$ DSNBs with a different mass ratio of 2H–$MoTe_2$ to S_v–In_2S_3 (1.0%, 3.0%, 5.0%, 7.0%, and 9.0%) were synthesized by adjusting the addition of $Na_2MoO_4·2H_2O$ and Te, and the synthesized samples were labeled as S_v–In_2S_3@2H–$MoTe_2$(1), S_v–In_2S_3@2H–$MoTe_2$(3), S_v–In_2S_3@2H–$MoTe_2$(5), S_v–In_2S_3@2H–$MoTe_2$(7), and S_v–In_2S_3@2H–$MoTe_2$(9), respectively. For comparison, the pure 2H–$MoTe_2$

nanosheets (NSs) were prepared following the above steps without adding S_v–In_2S_3 SSNBs.

2.3 Characterization

The crystal phase properties and morphologies for various samples were analyzed with an X-ray diffraction (XRD) and scanning electron microscopic (SEM) images, respectively. To further determine the morphology and crystal lattice structure of the materials, transmission electron microscopy (TEM) images were taken using a Hitachi H-7650 transmission electron microscope at an acceleration voltage of 100 kV. High-resolution TEM (HRTEM), high-angle annular dark-field scanning transmission electron microscopy (HAADF-STEM), and energy-dispersive X-ray spectroscope (EDX) mapping were carried out on a JEOL ARM-200F field-emission transmission electron microscope operating at 200 kV accelerating voltage. X-ray photoelectron spectroscopy (XPS, ESCALAB250) of Thermo was used to study the element combination and valence of the materials in this work. Temperature programmed desorption (TPD) profiles of the samples were recorded by a Micromeritics AutoChem II 2920 chemisorption analyzer with a thermal conductivity detector (TCD). The Brunauer–Emmett–Teller (BET) specific surface areas and porosity of the samples were determined using micromeritics (ASAP 2460 U.S.A.) surface area and porosity analyzer. The ultraviolet–visible diffuse reflectance spectra (DRS) were recorded using a UV–vis instrument (Japan). Steady-state photoluminescence (PL) and time-resolved photoluminescence (TRPL) spectra were collected on the F-7000 fluorescence spectrophotometer (Japan, Hitachi, $\lambda_{ex} = 319$ nm, $\lambda_{em} = 610$ nm) and FLS920 fluorescence lifetime spectrophotometer (Edinburgh Instruments, UK), respectively.

2.4 Photocatalytic CO_2RR Experiment

The photocatalytic CO_2RR measurement was conducted by the Lab Solar-III AG system (Perfect light Limited, Beijing). A 300 W Xe lamp equipped with a UV cut-off filter ($\lambda > 400$ nm) was adopted as the light source, calibrated by a CEL-NP2000 Optical Power Meter (Beijing China Education Au-light Co., Ltd.). The intensity of visible-light was 360 mW cm^{-2}. The instrument was initially vacuum-treated 3 times and then pumped with high-purity CO_2 to reach atmospheric pressure. 50 mL of $KHCO_3$ (0.5 M) was injected into this setup for further photocatalysis. Gas products were detected using a Barrier Discharge Ionization Detector (BID) detector with gas chromatography (Shimadzu, Nexis GC-2030). ^{1}H nuclear magnetic resonance (NMR) spectra were recorded on a Bruker DPX 400 spectrometer to detect the liquid products.

The specific operation for cycling experiments: at first, the cycling stability test was measured by repeating the above operations with a 20 mg sample every 5 h. During the light irradiation, the carbon-based gas products were qualitatively analyzed by Agilent GC7890B gas chromatograph by identifying the chromatographic peaks. Other gas products, such as O_2, were analyzed by a thermal conductivity detector. The carrier gas was Ar with a flow rate of 20 mL min^{-1}, and the column temperature was 393 K. All gas products were injected by an automatic online sampler with 1.0 mL gas. After the reaction, the liquid products were quantified by NMR spectroscopy, in which DMSO solution was used as the internal standard. The temperatures of the solutions were controlled at 298 ± 0.2 K by a recirculating cooling water system during visible-light irradiation [9].

2.5 Computational Details

First-principles computations based on the density functional theory (DFT) were implemented in the Vienna Ab initio simulation package (VASP) [10]. The generalized gradient approximation (GGA) involving Perdew, Burke, and Ernzerhof (PBE) was used for calculating the exchange–correlation energy [11]. A 400 eV of cut-off energy was adopted for the plane-wave basis set in conjunction with the projector augmented wave (PAW) [12]. The energy and force convergence were set to be 1×10^{-4} and 5×10^{-2} eV, respectively. Here, a vacuum layer of 12 Å is chosen in the z direction to avoid interactions between periodically repeated slabs. The Brillouin zone was sampled using the Monkhorst–Pack scheme, K-points were generated by VASPkit [13], and the recommended value is 0.04 ($2\pi \times 0.04$ Å^{-1}). The van der Waals interaction was considered by using the DFT-D3 method [14].

The Gibbs free energy of the intermediates for HER and CO_2RR process, that is, *CO_2, *OCHO, OH*, CO*, CHO*, CH_2O*, CH_3O*, and *O, can be calculated as follows:

 https://doi.org/10.1007/s40820-023-01221-3

$$\Delta G = \Delta E_{DFT} + \Delta E_{ZPE} - T\Delta S \quad (1)$$

$$\Delta E_{ZPE} = \Delta \sum_i 1/2\, hv_i \quad (2)$$

$$\theta_i = hv_i/\mathrm{k} \quad (3)$$

$$S = \sum_i R[\ln(1 - e^{-\Theta_i/T})^{-1} + \Theta_i/T(e^{\Theta_i/T} - 1)^{-1}] \quad (4)$$

where ΔE_{DFT}, ΔE_{ZPE}, and ΔS are the total energy change, zero-point energy change, and the entropy change (ΔS) of each adsorbed state were calculated according to the standard molar Gibbs energy of formation at 298.15 K. S is the entropy, h is the Planck constant, ν is the computed vibrational frequencies, Θ is the characteristic temperature of vibration, k is the Boltzmann constant, and R is the molar gas constant. T is the temperature and is taken as 298.15 K. The entropy of other adsorbed states ($T\Delta S$) is calculated from the vibrational frequencies associated with the standard modes in the harmonic approximation [15]. The contributions are listed (Tables S8 and S9). For adsorbates, E_{ZPE} and S are obtained from vibrational frequency calculations with harmonic approximation, and contributions from the slabs are neglected. In contrast, for molecules, these values are taken from NIST-JANAF thermochemical Tables [16].

3 Result and Discussion

3.1 Structural Characterization

The experimental sections and preparation procedure were provided in Supporting Information and Figs. S1–S3, including the synthesis of hollow In_2S_3 using Cu_2O NCs as a template and the subsequent hydrothermal synthesis S_v–In_2S_3 and 2H–$MoTe_2$. With regard to the electron paramagnetic resonance (EPR) spectrum, S_v–In_2S_3, and S_v–In_2S_3@2H–$MoTe_2$(5) represent a clear signal at $g = 2.076$ (Fig. S4a), further reconfirming that S_v–In_2S_3@2H–$MoTe_2$(5) and S_v–In_2S_3 are rich in S-vacancies species [2, 17]. Of great importance, the higher concentration of S-vacancies species in S_v–In_2S_3@2H–$MoTe_2$(5) leads to significant changes in its electronic structure, steric interaction of chemical bonds and energy density distribution, thereby significantly enhancing its electrical conductivity, which is more beneficial for electrons transfer during photocatalytic CO_2RR progress [18, 19]. As a comparison, there is no obvious S-vacancies signal of In_2S_3 in EPR spectrum. The XRD patterns of S_v–In_2S_3 and In_2S_3 are well indexed to the tetragonal phase of In_2S_3 (JCPDS No. 73-1366), indicating their high purity without any other crystal structure changes (Fig. 2a). Interestingly, S_v–In_2S_3 denote almost the same diffraction signals as the In_2S_3, and there are no other heterogeneous phases, which accounts for that the S-vacancies hardly affects original crystal phase structure of In_2S_3 [20]. Figure S5 exhibits that S_v–In_2S_3@2H–$MoTe_2$(5) possesses a micro/mesoporous structure with the size at range of 0–250 nm, and the average pore diameter is about 4.51 nm (Table S3). Furtherly, S_v–In_2S_3@2H–$MoTe_2$(5) has increased surface area that helps to increase contact with the reactants and shorten transmission path of the charge carrier [21]. According to above analysis, S_v–In_2S_3@2H–$MoTe_2$(5) has abundant catalytic active sites and porous structures, which is conducive to increase contact area with reactants, and facilitate escape of CH_4, CO, and H_2, thus improving photocatalytic CO_2RR activity.

The morphological characteristics of S_v–In_2S_3@2H–$MoTe_2$(5), S_v–In_2S_3, In_2S_3, and 2H–$MoTe_2$ were elaborately analyzed via SEM, TEM, HRTEM, HAADF-STEM, and HAADF-STEM-EDX elemental mapping images, respectively. As depicted in Fig. 1, the basic morphology of S_v–In_2S_3@2H–$MoTe_2$(5) is a double-shelled nanoboxes composed of a large number of ultrathin nanosheets on the exterior, which facilitates the exposure of active surface and the scattering phenomenon (Mie scattering) [22]. The EDX elemental mapping images of S_v–In_2S_3@2H–$MoTe_2$(5) present that Mo and Te elements are obviously distributed on the outer surface of S_v–In_2S_3 (Fig. 1g), illustrating the successful formation of homogeneous nano-heterojunction structures between S_v–In_2S_3 and 2H–$MoTe_2$, which can be further proved that 2H–$MoTe_2$ was directly grown and attached to S_v–In_2S_3. Besides, it can be clearly seen that atomic data ratio of In/S and Mo/Te is about 1.00/1.48 and 1.00/2.05 (Table S1), which is extremely close to stoichiometric ratio in molecular formula of In_2S_3 and 2H–$MoTe_2$. Furtherly, HRTEM images, inverse fast Fourier transform (IFFT) patterns, and lattice fringe profile (LFP) manifest distinctly visible lattice fringes with spacing of 2.47 and 2.20 Å (Fig. 1e), pointing precisely to (219) crystal plane of In_2S_3 (JCPDS:73-1366) and (104) crystal plane of 2H–$MoTe_2$ (JCPDS:73-1650), respectively. The selected-area-electron-diffraction (SAED) pattern of S_v–In_2S_3@2H–$MoTe_2$(5) reveals a ring-like pattern

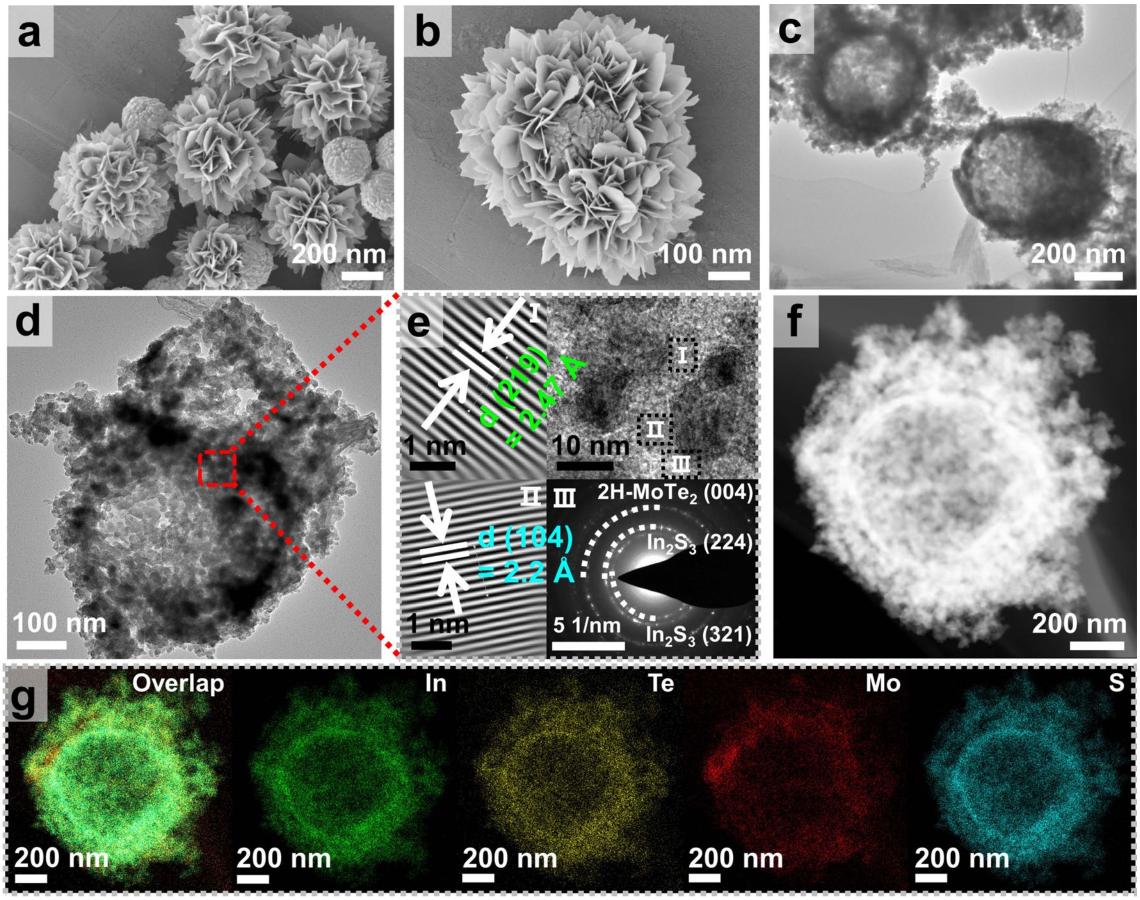

Fig. 1 **a, b** SEM, **c, d** TEM, **e** HRTEM images, IFFT (top) and SAED patterns, **f** HAADF STEM, and **g** HAADF-STEM-EDS elemental mapping images of S_v–In_2S_3@2H–$MoTe_2$(5), respectively

of S_v–In_2S_3 and 2H–$MoTe_2$, confirming the presence of S-vacancies and polycrystalline features of composites.

3.2 Electronic Structure Analysis

The chemical composition and atomic state information of samples were compared by XPS. The complete scanning spectrogram is shown in Fig. S4b–f, and the specific atomic ratio is displayed in Table S2. In the Mo 3*d* core-level spectrum in Fig. S4e, the peaks of $3d_{5/2}$ and $3d_{3/2}$ appear on 225.7 and 229.0 eV, belonging to Mo–S bridging bonds in S_v–In_2S_3@2H–$MoTe_2$(5) [23]. The binding energies (B. E.) of Mo^{4+} at 227.9 and 231.1 eV in 2H–$MoTe_2$ negatively shift to 225.7 and 228.9 eV in S_v–In_2S_3@2H–$MoTe_2$(5). It is speculated that the uniform distribution of S-vacancies in S_v–In_2S_3 regulates the coordination environment of 2H–$MoTe_2$, leading to a change in d-band electronic state of Mo [24]. The peaks at 159.1 and 161.6 eV in S 2*p* spectrum (Fig. S4f) represent S $2p_{3/2}$ and S $2p_{1/2}$ binding energies of S^{2-} in S_v–In_2S_3@2H–$MoTe_2$(5). The slight positive shift of S 2*p* peak (by 1.47 eV) is also attributed to the interfacial charge transfer of S_v–In_2S_3 and 2H–$MoTe_2$ [25, 26]. The negative shift of S 2*p* and positive shift of Mo^{4+} indicate the charge transfer from 2H–$MoTe_2$ to S_v–In_2S_3 at S_v–In_2S_3@2H–$MoTe_2$(5) (Fig. S4c). The X-ray absorption fine structure spectroscopy (XAFS) of Mo K-edge and In K-edge was employed to provide in-depth insights into atomic and electronic structure between S_v–In_2S_3 and 2H–$MoTe_2$ in S_v–In_2S_3@2H–$MoTe_2$(5). Figure 2b reveals the X-ray absorption near-edge structure (XANES) spectrum at Mo K-edge of samples along with Mo metal foil and MoS_2 standard. In Mo and MoS_2, Mo exit in 0 and +4 oxidation states, respectively [27, 28]. The absorption edge of samples lies between that of Mo metal foil and MoS_2. The

 https://doi.org/10.1007/s40820-023-01221-3

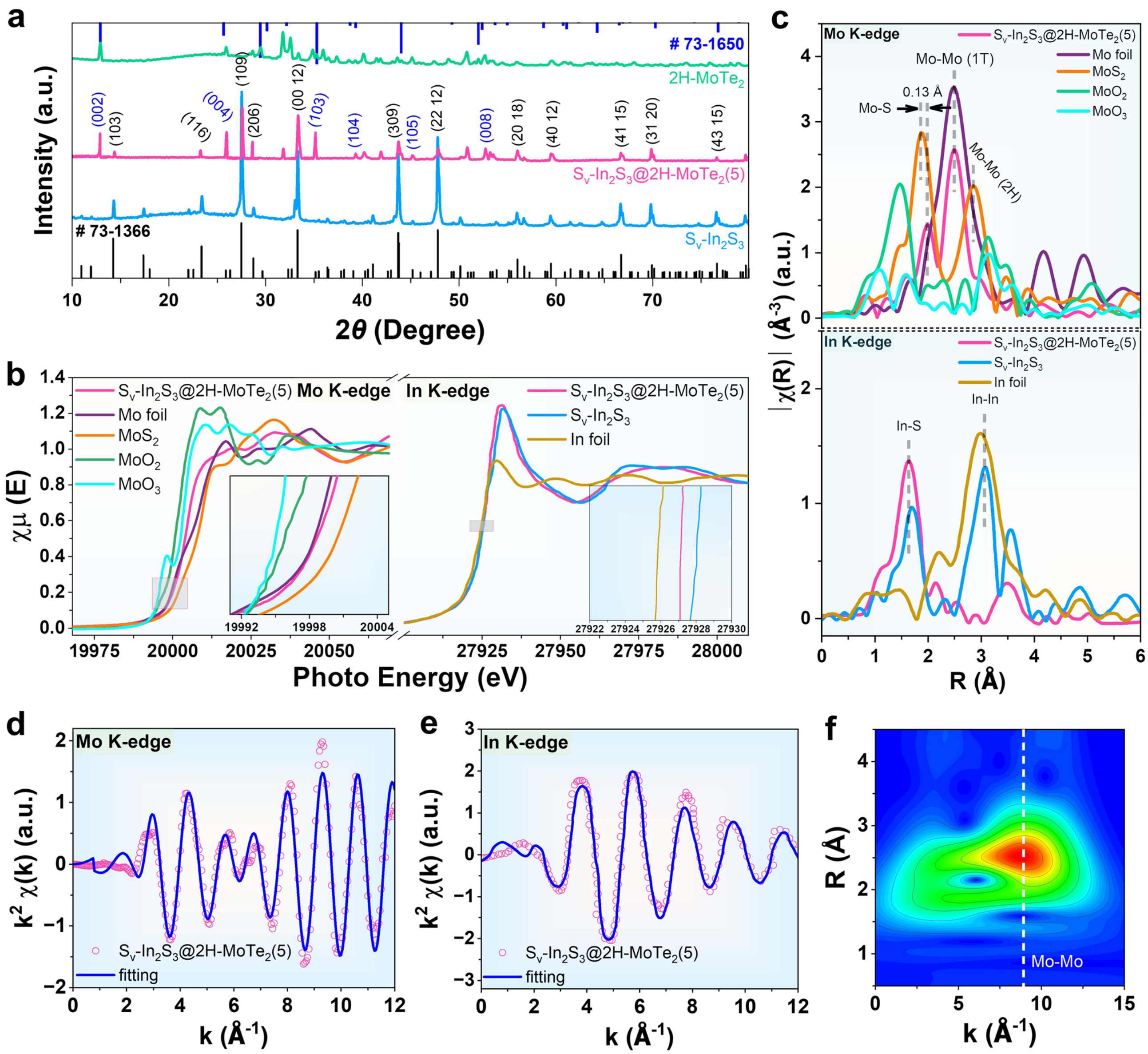

Fig. 2 **a** XRD patterns of 2H–$MoTe_2$, In_2S_3, S_v–In_2S_3, and S_v–In_2S_3@2H–$MoTe_2$(5), respectively. **b** Comparison of Mo and In K-edge XANES spectra. **c** k^3-weighted FT-EXAFS spectra of Mo and In at R space. **d** Mo K-edge EXAFS and **e** In K-edge EXAFS for S_v–In_2S_3@2H–$MoTe_2$(5), shown in k^2 weighted k-space. **f** WT for k^3 weighted EXAFS contour plots of S_v–In_2S_3@2H–$MoTe_2$(5)

Mo K-edge XANES spectrum of S_v–In_2S_3@2H–$MoTe_2$(5) demonstrates a negative shift in contrast with that of MoS_2. The Mo valence of Mo–S bonds in S_v–In_2S_3@2H–$MoTe_2$(5) discloses a slight increase, corresponding with XPS results. The In K-edge XANES spectra of S_v–In_2S_3@2H–$MoTe_2$(5) and S_v–In_2S_3, showed the + 3 valence state of In element in S_v–In_2S_3@2H–$MoTe_2$(5) and S_v–In_2S_3 (Fig. 2b). The In EXAFS spectra shows the dominant peaks at 1.67 and 1.77 Å, corresponding to In – S and In–In coordination (Fig. 2c), respectively, which is consistent with XPS results (Fig. S12c). As observed in Figs. 2d, f and S6a, b, the extended X-ray absorption fine structure (EXAFS) spectrum for Mo sites shows two prominent peaks contributed by Mo–S and Mo–Mo bonds at 1.99 and 2.85 Å, respectively, implying the existence of Mo–S bridging bonds in S_v–In_2S_3@2H–$MoTe_2$(5) [29, 30]. Furthermore, the Mo K-edge EXAFS spectrum of S_v–In_2S_3@2H–$MoTe_2$(5) demonstrates a positive radial distance shift (0.13 Å) of Mo–S bonds compared to MoS_2, further confirming the existence of Mo–S bridging bonds [31, 32]. In 2D color patch image obtained after EXAFS signal via wavelet transformation (WT), a high energy signal (red area) appears at 8.5 Å for S_v–In_2S_3@2H–$MoTe_2$(5) (Fig. 2f) and MoS_2 (Fig. S6c), which corresponds to signal of Mo–Mo coordination bond [24, 33].

The difference in charge density between S_v–In_2S_3 and 2H–$MoTe_2$ can visually reflect the carrier transfer. In Fig. 4h and Fig. S14d, 3D charge density difference of S_v–In_2S_3@2H–$MoTe_2$(5) presented the existence of interfacial charge transfer between S_v–In_2S_3 and 2H–$MoTe_2$. It can be found from illustration that, the carriers are spontaneously transferred from S_v–In_2S_3 to 2H–$MoTe_2$ through the boundary, whereas holes gather on the side of S_v–In_2S_3 in S_v–In_2S_3@2H–$MoTe_2$(5). Consequently, the charge accumulation occurred on 2H–$MoTe_2$, whereas charge loss was observed on S_v–In_2S_3 [34]. Finally, a strong built–In electric field (IEF) of Mo–S bonds from S_v–In_2S_3 to 2H–$MoTe_2$ is established on account of the redistribution of electrons after the contact between S_v–In_2S_3 and 2H–$MoTe_2$ [35]. The interfacial electrostatic interaction allows the electrons in conduction band (CB) of 2H–$MoTe_2$ to recombine with the holes in valence band (VB) of S_v–In_2S_3 through Mo–S bridging bonds, resulting in effective retention of electrons in CB of S_v–In_2S_3.

3.3 Photocatalytic CO_2RR Performance

CO_2-TPD experiments were carried out on the photocatalyst to further explore the adsorption of CO_2. Figure 3a presents CO_2-TPD profiles of 2H–$MoTe_2$, S_v–In_2S_3, and S_v–In_2S_3@2H–$MoTe_2$(5), revealing the presence of prominent peaks in investigated temperature range and thus suggesting moderately primary CO_2 adsorption centers on the surface of photocatalyst. The hollow porous nature of S_v–In_2S_3@2H–$MoTe_2$(5) (Fig. S5) enables high CO_2 capture capability (36.83 $cm^3\ g^{-1}$, Fig. 3b), facilitating CO_2RR on S_v–In_2S_3@2H–$MoTe_2$(5). Herein, the higher CO_2 adsorption capacity of S_v–In_2S_3@2H–$MoTe_2$(5) is due to its chemisorption for CO_2 through the stronger coordination interaction of CO_2 with Mo (+4) (Scheme 1, Mo–S bridging bonds). The photocatalytic CO_2RR activity was evaluated via analyzing raw material and gas products produced at gas–solid interface in the absence of cocatalysts and photosensitizers (Fig. S7). The main products were examined by gas chromatography–mass spectra (GC–MS). During photocatalytic CO_2RR process, the principal reduction products in system are CO, CH_4, and H_2, which is consistent with the previous reports in similar scenarios. The S_v–In_2S_3@2H–$MoTe_2$(5), In_2S_3, and S_v–In_2S_3 show relatively lower photocatalytic CO_2RR activity, with CH_4-evolution rates of 13.97, 1.53, and 2.32 μL h^{-1}, respectively (Figs. 3d, e and S8a), nevertheless, 2H–$MoTe_2$ can hardly photocatalytic CO_2RR, in good accordance with above characterizations. In particular, the CO_2-to-CH_4 conversion rate of S_v–In_2S_3@2H–$MoTe_2$(5) reaches up to 70% (CH_4 selectivity: 79.6%) with an optimum apparent quantum efficiency (AQE) value of 16.5% at 420 nm (Fig. S8b), which is comparable to most reported CO_2-to-CH_4 conversion rate at similar reaction conditions (Fig. S8c and Table S10). The remarkable CO_2-to-CH_4 conversion efficiency of S_v–In_2S_3@2H–$MoTe_2$(5) can mainly be due to the Mo–S bridging bonds and robust built-IEF. As depicted in Fig. S8d, the variation tendency of CO, H_2, and CH_4 production are consistent with characteristic absorption spectrum of S_v–In_2S_3@2H–$MoTe_2$(5), which strongly sustains that photocatalytic CO_2RR is driven via the inter-band transition electrons of S_v–In_2S_3@2H–$MoTe_2$(5). Moreover, the control experiments in different conditions (Fig. 3c) confirm that the detected products are indeed derived from the reaction between CO_2 and H_2O, catalyzed by the samples, which is further affirmed via the result of $^{13}CO_2$ labeling experiment in Fig. S9. Compared with pristine In_2S_3, S_v–In_2S_3 with rich S-vacancies exhibits superior performance and excellent long-term stability. The photocatalytic performance of S_v–In_2S_3@2H–$MoTe_2$(5) was also tested in pure water. The production rate of CH_4 decreased in pure water as compared with those (Fig. S10).

As displayed in Fig. 3f, the calculated data present higher values for AQE analysis of S_v–In_2S_3@2H–$MoTe_2$(5) at different wavelengths, compared with than that of 2H–$MoTe_2$, In_2S_3, and S_v–In_2S_3 (See Table S8 for details of the calculation results), further evaluating photocatalytic CO_2RR activity. Moreover, S_v–In_2S_3@2H–$MoTe_2$(5) displays the highest AQE (65.29%) at 380 nm, being higher than most reported values (Table S9). Assisted by the robust built-IEF and Mo–S bonds of S_v–In_2S_3@2H–$MoTe_2$(5), "S"-scheme charge separation is notably facilitated, resulting in an IQE calculated via photocatalytic CO_2RR of 94.01% (IQE_{cr}) at 380 nm. This phenomenon proves the effective utilization of Mo–S bridging bonds and a breakthrough in IQE

 https://doi.org/10.1007/s40820-023-01221-3

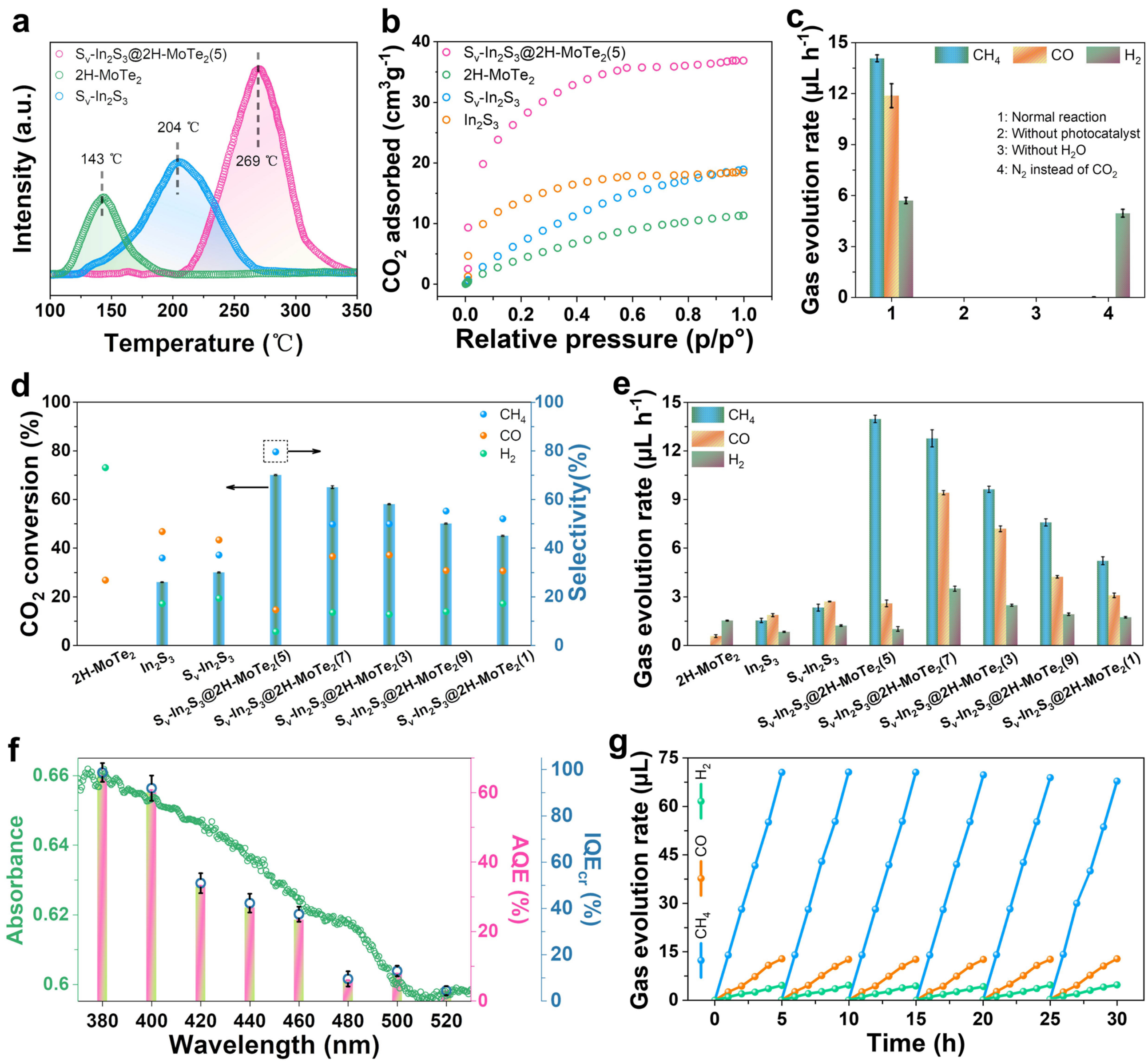

Fig. 3 **a** CO_2-TPD spectra of S_v–In_2S_3, 2H–$MoTe_2$, and S_v–In_2S_3@2H–$MoTe_2$(5), respectively. **b** CO_2 adsorption isotherms of samples at 298 K. **c** Control experiments in several conditions. **d** CO_2 conversion and product selectivity. **e** Yields of CO, CH_4, and H_2 for photocatalysts ($KHCO_3$ solution). **f** AQE, IQE_{cr}, and absorption spectrum of S_v–In_2S_3@2H–$MoTe_2$(5). **g** Stability test of with S_v–In_2S_3@2H–$MoTe_2$(5) in 6 cycles, where each photocatalytic cycle lasted for 5 h ($KHCO_3$ solution). All the experiments were repeated at least 3 times in parallel to obtain an average value

for S_v–In_2S_3@2H–$MoTe_2$(5) (Table S7). More specifically, cycling stability is also an important index to assessed the performance of photocatalyst in practical commercial use. Therefore, the stability of S_v–In_2S_3@2H–$MoTe_2$(5), S_v–In_2S_3, 2H–$MoTe_2$, and In_2S_3 was evaluated via cyclic stability tests in this work, respectively. As displayed in Fig. 3g, there is no remarkable decrease in evolution of CH_4, CO, and H_2, after 6 cycles of reaction using S_v–In_2S_3@2H–$MoTe_2$(5). According to the XRD patterns and TEM images (Fig. S11a–c) after 6 cycles test, the morphology and crystal structure of S_v–In_2S_3@2H–$MoTe_2$(5) have not changed significantly. Especially, XPS and EXAFS measurement was further used to study the change in chemical composition and atomic state before and after CO_2RR

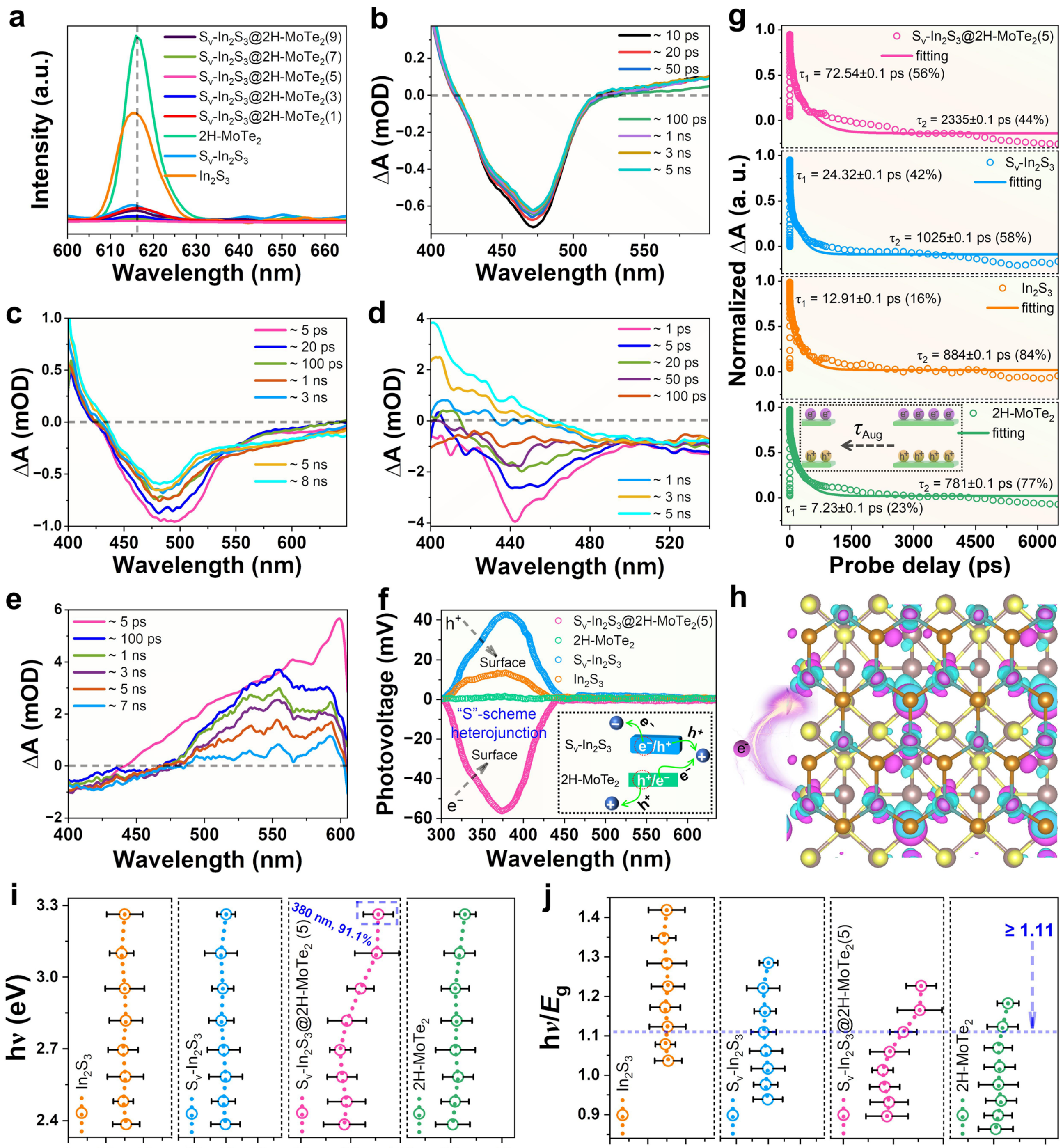

Fig. 4 **a** PL spectra of samples (excitation wavelength = 300 nm). Fs-TA spectra of **b** S_v–In_2S_3, **c** In_2S_3, **d** 2H–$MoTe_2$, and **e** S_v–In_2S_3@2H–$MoTe_2$(5) measured at different delay times, respectively (320 nm excitation). **f** SPV spectra of samples. **g** Comparison of normalized exciton bleach signal decay between S_v–In_2S_3 and 2H–$MoTe_2$ (the curves were fitting results using Equation S1 and S2). **h** Differential charge density map of S_v–In_2S_3@2H–$MoTe_2$(5) (magenta area (positive value) and cyan area (negative value) represent accumulation and consumption of electrons, respectively). **i** IQE_{pc} as a function of illumination photon energy for samples. **j** IQE_{pc} as a function of multiples of bandgap ($h\upsilon/E_g$) of samples for samples (mean values with error bars showing s.d. for 3 measurements)

Table 1 Carrier transport characteristics of samples

Samples	Bandgap (E_g, eV)	Fs-TA lifetime (ps)	TRPL lifetime (ns)	Carrier concentration (n, cm^{-3})	Mobility [cm^2 V^{-1} s^{-1}]	Diffusion length [L_d, μm]	IQE_{cr} (%)
S_v–In_2S_3@2H–$MoTe_2$(5)	2.66	$\tau_1=12.3$, $\tau_2=2335$	$\tau_1=12.3$, $\tau_2=22.6$	4.51×10^{13}	2.38	0.26–0.36	94.01
S_v–In_2S_3	2.54	$\tau_1=24.32$, $\tau_2=1025$	$\tau_1=11$, $\tau_2=15$	2.68×10^{13}	1.64	0.2–0.24	12.88
In_2S_3	2.30	$\tau_1=12.91$, $\tau_2=884$	$\tau_1=1.6$, $\tau_2=9.8$	9.4×10^{12}	0.99	0.06–0.15	11.76
2H–$MoTe_2$	2.76	$\tau_1=7.23$, $\tau_2=781$	$\tau_1=0.98$, $\tau_2=4.4$	1.03×10^{12}	0.27	0.025–0.05	10.51

*n.d. not determined

(Figs. S11d, e and S12). Noteworthily, there is no peak shift in S_v–In_2S_3@2H–$MoTe_2$(5) after cyclic stability test. The above experimental results and analysis can prove outstanding morphology and structure of S_v–In_2S_3@2H–$MoTe_2$(5).

3.4 Photoelectric Performance Analysis

We evaluate the recombination of charge carriers through steady-state PL, ultrafast femtosecond transient absorption (fs-TA) spectroscopy, and TRPL spectra to study photocatalytic CO_2RR activity. Clearly, 2H–$MoTe_2$ exhibits strongest emission peak is corresponding to the rapid recombination of electrons-holes pairs (Fig. 4a), suggesting enhanced electronic conductivity of S_v–In_2S_3@2H–$MoTe_2$(5). Among them, S_v–In_2S_3@2H–$MoTe_2$(5) illustrates the weakest emission peak, consistent with their optimal photocatalytic CO_2RR performance [36]. The fs-TA spectroscopic experiments were carried out on S_v–In_2S_3@2H–$MoTe_2$(5) exited at $\lambda=320$ nm in CO_2 atmosphere to further gain insight into electrons transfer dynamics during photocatalytic CO_2RR process. For the purposes of comparison, we also recorded fs-TA spectra of S_v–In_2S_3, In_2S_3, and 2H–$MoTe_2$ under the same test condition. After excitation of S_v–In_2S_3, a bleaching peak was observed at 474 nm, and the peak strength decreased with increasing delay time, which indicated that the recombination of a fraction of electrons and holes occurred in S_v–In_2S_3 with prolonged delay time (Fig. 4b). Similar phenomenon is obtained for In_2S_3 (Fig. 4c), indicating that the relaxation process of S_v–In_2S_3@2H–$MoTe_2$(5) and S_v–In_2S_3 under bandgap excitation is similar. For 2H–$MoTe_2$, the strong and broad photoinduced bleaching peaks are observed at 442 nm, which is attributed to the generation of photoexcited holes in VB of 2H–$MoTe_2$ [37, 38]. As delay time increased to 3 ns, these peaks are not observed in 2H–$MoTe_2$ owning to the recombination of electrons and holes (Fig. 4d). Noteworthily, when S_v–In_2S_3 was introduced into 2H–$MoTe_2$, the peak strength of S_v–In_2S_3 at 475 ~ 550 nm increased with increasing delay time (Fig. 4e, h), indicating that electrons transfer from 2H–$MoTe_2$ to S_v–In_2S_3 [37], which is completely consistent with the analysis results in Figs. S13–S15a. More specifically, the energy band structure of S_v–In_2S_3 is in good agreement with that of 2H–$MoTe_2$, and can attain the thermodynamic conditions for the spontaneous photocatalytic CO_2RR process. The analysis of recovery kinetics discloses that the best decay fitting provides a bi-exponential function with two-time constants of $\tau_1=72.54$ ps and $\tau_2=2335$ ps for S_v–In_2S_3@2H–$MoTe_2$(5) (Fig. 4g). The τ_1 and τ_2 are attributed to the electron dynamics related to different electronic trap states with energies lie within the bandgap of S_v–In_2S_3@2H–$MoTe_2$(5). These two near-band edge trap states accumulate photogenerated electrons from bottom of CB in a bi-exponential relaxation (Fig. S15a) [39]. The longer carrier lifetime and stronger positive absorption of S_v-In_2S_3@2H-$MoTe_2$(5) are further evidenced via the Hall effect measurement. The Hall effect measurement at 300 K reveals that S_v-In_2S_3@2H-$MoTe_2$(5) possesses a carrier concentration of 4.51×10^{13} cm^{-3}, an estimated carrier mobility of 2.38 cm^2 V^{-1} s^{-1} (Table 1). The TRPL spectra in Fig. S15b and Table S6 display that S_v–In_2S_3@2H–$MoTe_2$(5) presents longer retention time (20.8 ns) of photoinduced carriers than that of S_v–In_2S_3 (9.2 ns) due to the introduction of 2H–$MoTe_2$ (179 ns), which further demonstrates the effective restraining effect to electrons-holes recombination. The carrier diffusion lengths (L_d) are estimated to be in range of 0.26–0.36 μm for S_v–In_2S_3@2H–$MoTe_2$(5), and 0.025–0.05 μm for 2H–$MoTe_2$, respectively (Table 1). Besides, the surface photovoltage (SPV) spectra were also conducted to validate its carrier transfer mechanism, as shown in Fig. 4f.

It is noted that 2H–$MoTe_2$ present no SPV signals in whole wavelength, illustrating the poor photocarrier separation efficiency. That's why 2H–$MoTe_2$ perform extremely poorly CO_2RR activity. In comparison, a significant positive photovoltage response can be observed in SPV spectra of In_2S_3 and S_v–In_2S_3, illustrating that the holes migrate to the surface of In_2S_3 and S_v–In_2S_3, which is a typical trait of n-type semiconductors. Besides, in SPV spectra, unlike the positive photovoltage signal of 2H–$MoTe_2$ and S_v–In_2S_3, a negative and significantly enhanced photovoltage signal at 300–430 nm emerged in S_v–In_2S_3@2H–$MoTe_2$(5), demonstrating that the photogenerated electrons of S_v–In_2S_3 and holes of 2H–$MoTe_2$, transferred to illumination side and backlight side, respectively, and the remained electrons of 2H–$MoTe_2$ recombined with holes of S_v–In_2S_3 through a built-IEF, which further reveals the efficient interfacial charge transfer within the heterojunction via a "S"-scheme pathway.

The incident photon-to-current efficiency (IPCE) and corresponding IQE_{pc} were measured under different wavelengths of monochromatic light irradiation to investigate the photoelectric conversion efficiency of S_v–In_2S_3@2H–$MoTe_2$(5) [40]. The IPCE profiles of S_v–In_2S_3@2H–$MoTe_2$(5) at different wavelengths are consistent with the above optical absorption results (Fig. S15c), verifying excellent carrier transfer and separation. The IQE_{pc} was assessed by normalizing the IPCE values to the measured absorption curve of S_v–In_2S_3@2H–$MoTe_2$(5), S_v-IS SSNBs, In_2S_3, and 2H–$MoTe_2$. The IQE_{pc} curves of S_v–In_2S_3, In_2S_3, and 2H–$MoTe_2$ remain flat in total wavelength range (380–520 nm), while the IQE_{pc} curves of S_v–In_2S_3@2H–$MoTe_2$(5) show an upward trend when S_v–In_2S_3 and 2H–$MoTe_2$ were combined to form Mo–S bridging bonds (Fig. 4i, j). Intriguingly, the S_v–In_2S_3@2H–$MoTe_2$(5) discloses the maximum IQE_{pc} value of 91.1% at 320 nm, indicating enhanced exciton extraction force driven by a strong built-IEF at the interface between S_v–In_2S_3 and 2H–$MoTe_2$. To further validate our perception, the IQE_{pc} curves vs. E_g of S_v–In_2S_3@2H–$MoTe_2$(5), S_v–In_2S_3, In_2S_3, and 2H–$MoTe_2$ are plotted to elucidate the photon absorption and conversion in S_v–In_2S_3@2H–$MoTe_2$(5). The IQE_{pc} of S_v–In_2S_3@2H–$MoTe_2$(5) gradually increases when the incident photon energy exceeds 1.11 times the E_g of 2H–$MoTe_2$, significantly promoting charge transport and separation within S_v–In_2S_3@2H–$MoTe_2$(5), which is mainly due to possibility of multiple exciton production in 2H–$MoTe_2$ [41].

3.5 Relationship Between Mo–S Bridging and CO_2RR Activity

In situ diffuse reflectance–Infrared Fourier transform spectroscopy (DRIFTS) and in situ high-resolution XPS spectroscopy were performed to correlate surface characteristics to the efficiency of photocatalytic CO_2RR progress. The analysis results are shown in Fig. 5. From 0 to 60 min, new absorption peaks perceptibly appear with increasing light time and their intensity gradually increase. The observation of new infrared peak at 1127 cm^{-1} gradually increases, which can be ascribed to the CH_3O^* intermediates (the asterisk denotes the catalytically active sites), while the peak at about 1040 cm^{-1} can be assigned to the characteristic bands of CHO*. The peaks at 1560 and 1630 cm^{-1} are attributed to the COOH*, which is generally regarded as the key intermediates of CO_2 photoreduction to CH_4 or CO, as well CH_3OH [42, 43]. The peaks at 1430 cm^{-1} are corresponded to symmetric stretching of HCO_3^*, respectively. The formation of monodentate carbonate (m-CO_3^{2-}) and bidentate carbonate (b-CO_3^{2-}) are evidenced from infrared peaks of around 1368 and 1329 cm^{-1}, respectively (Fig. 5a) [44, 45]. Similar phenomenon is obtained for S_v–In_2S_3 (Fig. 5b). The in situ XPS was used to study changes of hydrocarbons on the surface of S_v–In_2S_3@2H–$MoTe_2$(5) during photocatalytic CO_2RR process. In dark state, no peak of gas-phase CH_4 (286.9 eV) is observed (Fig. 5c, d), illustrating that photoreduction of CO_2–CH_4 is light-driven. In contrast, with the gradual increase of light, a peak of surface-CH_x species appears at about 285.8 eV, further supporting the dissociation of generated CH_4 at the surface of catalyst to form H_2, which is why we detected the presence of H_2 product in mixing products.

In terms of the above analyses, the DFT simulations were performed to gain in-depth insights into Mo–S bridging bonds mechanism toward CO and CH_4 products on S_v–In_2S_3@2H–$MoTe_2$(5). In this research, in order to more accurately explain thermodynamic process of photoreduction of CO_2–CO, H_2, and CH_4, we introduced S-vacancies into structure of In_2S_3 under visible-light irradiation and determined the most optimal position for S-vacancies to participate in photocatalytic reaction (Fig. S22). Initially, CO_2 will be gradually adsorbed on the surface of S_v–In_2S_3@2H–$MoTe_2$(5), and H_2O in solution will be concomitantly dissociated and produce hydroxide ions (OH^-) and H^+. It is worth noting that path 1 is an endothermic

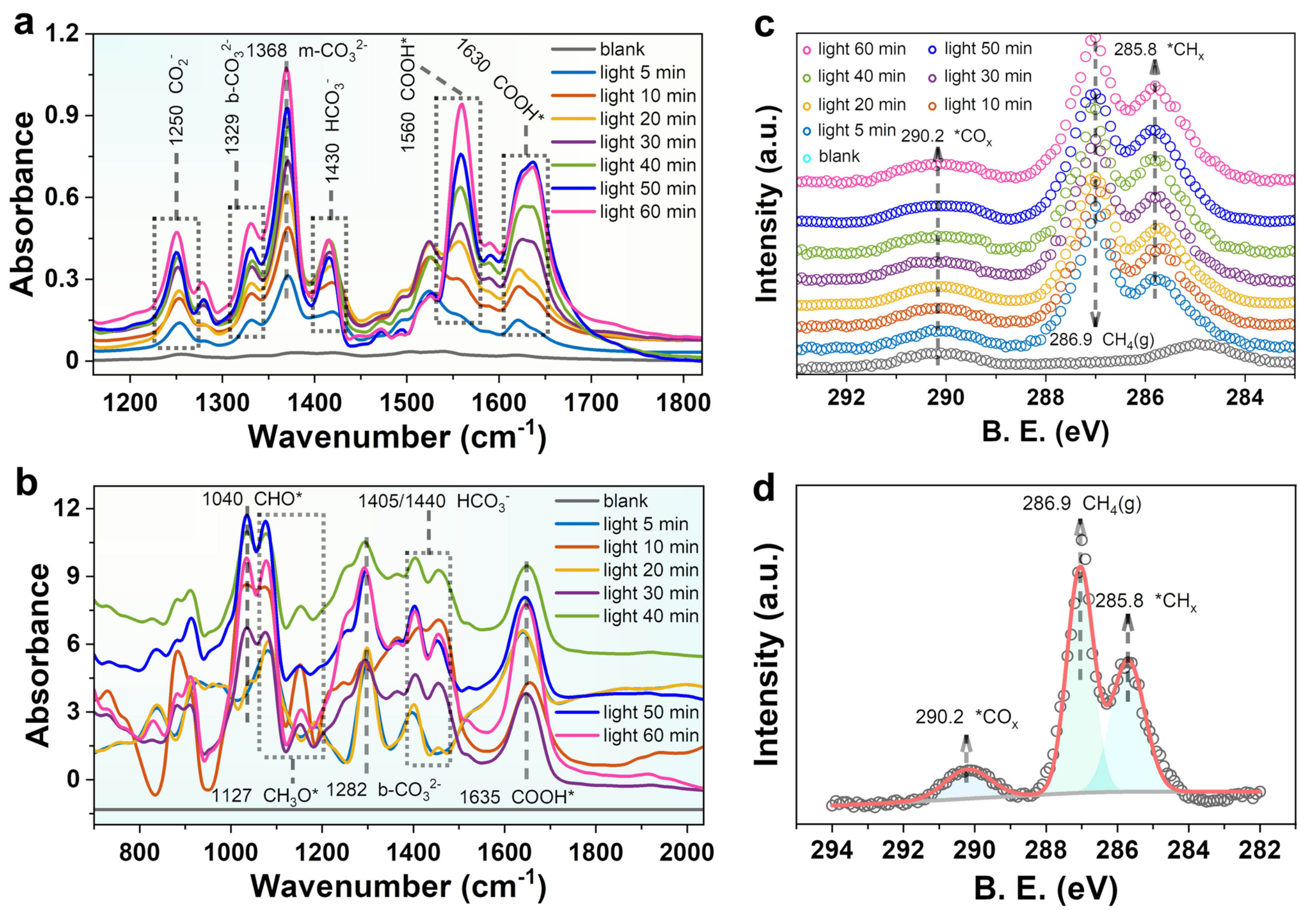

Fig. 5 In situ DRIFTS spectra for photocatalytic CO_2RR over **a** S_v–In_2S_3@2H–$MoTe_2$(5) and **b** S_v–In_2S_3. **c** In situ high-resolution C 1*s* XPS spectra of S_v–In_2S_3@2H–$MoTe_2$(5) with different light illumination time. **d** C 1*s* near ambient pressure XPS (NAP-XPS) collected for CH_4 conversion over S_v–In_2S_3@2H–$MoTe_2$(5) under light illumination at 5 min

during the reaction ($\Delta G > 0$), so it is not considered here (Fig. S23). The Gibbs free energy analysis curves for photocatalytic CO_2-to-CH_4 process (path 2) with the lowest energy pathway on the surface of S_v–In_2S_3@2H–$MoTe_2$(5) was calculated in detail, as shown in Fig. 6. During reaction process of photocatalytic CO_2RR to form CO, H_2, and CH_4, seven intermediate products can be produced, which are *OCHO, OH*, CHO*, CH_2O*, CO*, O*, and CH_3O*, respectively. The other *CO on the surface diffuse toward S-vacancies and couple with those reaction intermediates to produce CH_4 (Fig. 6a, b). The CH_4 free energy diagrams are summarized in Fig. 6c, while the corresponding minimum energy reaction pathways are presented in Fig. 6d. The diagram of free energy calculations illustrates that the reaction process of *OCHO–CO(g) and *OH is a potentially decisive step ($\Delta G = -0.84$ eV). Initially, the CO_2 energetically favor Mo–S bridging bonds sites from CO_2–CO. When one H atom approaches the adsorbed CO_2, it can form *OCHO [46]. Noteworthily, the S-vacancies can promote activation of CO_2, reduce energy barrier for the formation of *OCHO, and promote charge transfer to *OCHO, thereby promoting CO_2RR to form CO [47]. Furtherly, the formation of *OCHO is the step with the highest energy barrier in the formation of final CH_4, and thus, the *OCHO will transition to OH*. The ΔG of CO* desorption is around −0.51 eV lower than that of CHO* (Fig. 6c and Fig. S18a), resulting in a mixture of final products with CO, H_2, and CH_4 at Mo–S bridging bonds sites during CO_2RR process. It should be emphasized that CO desorption on S_v–In_2S_3@2H–$MoTe_2$(5) is an exothermic process. In contrast, the hydrogenation of CO*–CHO* is spontaneously exothermic, namely $\Delta G < 0$, resulting in a better selectivity for photoreduction of

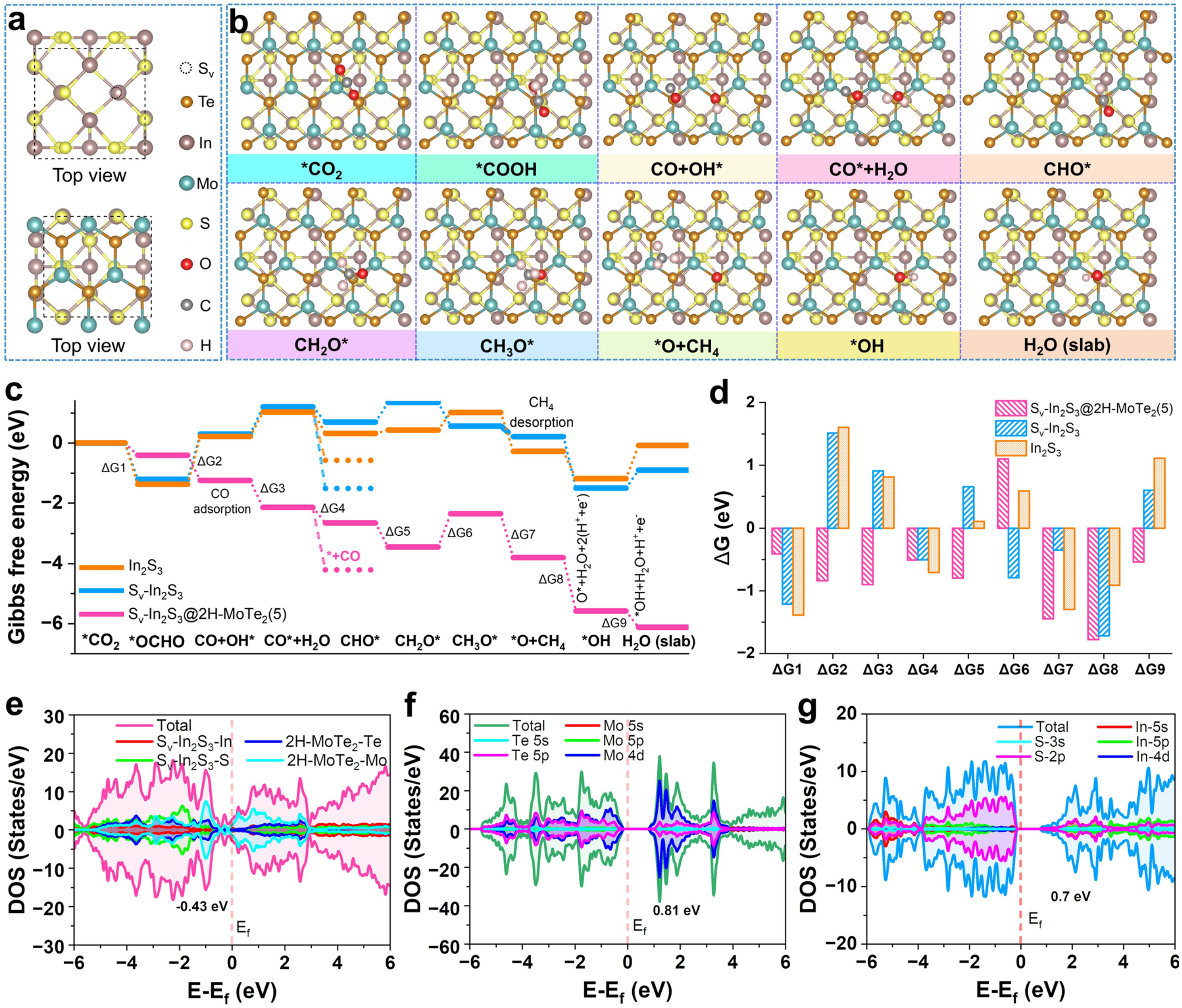

Fig. 6 **a** Atomic models of S_v–In_2S_3@2H–$MoTe_2$(5) in theoretical calculations. **b** Schematic illustration of adsorption atomic structures during CO_2RR process on over S_v–In_2S_3@2H–$MoTe_2$(5) interfaces. **c** Schematic Gibbs energy profiles and **d** energy changes for CO_2RR pathway at 1.23 V on different active sites for S_v–In_2S_3@2H–$MoTe_2$(5), S_v–In_2S_3, and In_2S_3, respectively. The calculated DOS of **e** S_v–In_2S_3@2H–$MoTe_2$(5), **f** 2H–$MoTe_2$, and **g** S_v–In_2S_3

CO_2–CO, which perfectly accords with above results analysis of the CO_2-TPD (Fig. 3a).

We also explored reaction energy barriers of S_v–In_2S_3@2H–$MoTe_2$(5) for H_2O splitting under alkaline conditions. As shown in Fig. S18a–c, we constructed the reaction path of alkaline HER, including previous water dissociation to the formation of H* (Volmer step) and H_2 generation (Tafel step or Heyrovsky step). The 2H–$MoTe_2$ shows the highest H–OH adsorption energy ($\Delta G_{ads} = 1.21$ eV) and H* adsorption energy barrier ($\Delta G_{H*} = 0.55$ eV), suggesting that the strong H* adsorption energy of In_2S_3 will hinder the evolution of H_2, resulting in slow HER kinetics, which is consistent with the experimental results (Fig. 3e). The d-band center position of catalysts is an important factor that determines the adsorption energy of intermediates. Significantly, the combined analysis of free energy and density of state (DOS) calculations and electrostatic potentials simulation present apparent evidence for step-by-step reactions of S_v–In_2S_3, In_2S_3, and S_v–In_2S_3@2H–$MoTe_2$(5) promoted via modulation of active sites and electronic structures [48]. An upshifted d-band center toward Fermi level reveals enhanced adsorption of intermediates. This is duo to the higher energy level of the d-band center allows for stronger interaction between photocatalyst and intermediates, leading to more efficient photocatalytic CO_2RR [49]. The S_v–In_2S_3@2H–$MoTe_2$(5) has a significantly upshifted d-band center (− 0.43 eV) compared to S_v–In_2S_3 (0.70 eV) and 2H–$MoTe_2$ (0.81 eV) (Fig. 6e – g), illustrating that S_v–In_2S_3@2H–$MoTe_2$(5) should possess a stronger binding strength for CO_2RR intermediates. Herein, we demonstrate that the introduction of Mo–S bridging bonds to construct heterogeneous structures tailors the d-band center, which in turn affects the adsorption capacities of different intermediates (Scheme 1) and ultimately optimizes CO_2RR activity. The cyan and magenta regions indicate electron depletion and accumulation (Figs. 4 h and S14d), respectively. This result can be derived from influence of S-vacancies on the electronic structure of enhanced damage prevention in S_v–In_2S_3@2H–$MoTe_2$(5) interfaces.

4 Conclusion

In summary, inspired by the construction of a strong IEF that can elevate d-band center to Fermi level, we elaborately designed a double-shelled nanoboxes structure, an ultrathin 2H–$MoTe_2$ coated S_v–In_2S_3 to form Mo–S bridging bonds sites for CO_2RR. The in situ characterization and DFT calculations affirmed that a strong interfacial electric field of S_v–In_2S_3@2H–$MoTe_2$(5) can reduce adsorption energy barriers of *OCHO and *CHO, and significantly enhance reaction rate of the rate-determining step on the surface of Mo–S bridging bonds. The S-vacancies can promote activation of CO_2, reduce energy barrier for the formation of *OCHO, and promote charge transfer to *OCHO, thereby promoting CO_2RR to form CO. Furthermore, the charge difference leads to the formation of polarization sites of Mo at the interface, which inhibits the electrostatic repulsion of adjacent intermediates and promotes formation of CO and CH_4.This study reveals that the interfacial electric field in S_v–In_2S_3@2H–$MoTe_2$(5) can obviously facilitate CO_2RR via tuning the d-band center of Mo and adsorption of intermediates, which provides a guideline for future rational fabrication and construction of catalysts for CO_2RR and other related reactions.

Acknowledgements This work is supported by the Natural Science Foundation of China (11922415, 12274471), Guangdong Basic and Applied Basic Research Foundation (2022A1515011168, 2019A1515011718, 2019A1515011337), the Key Research and Development Program of Guangdong Province, China (2019B110209003).

Funding Open access funding provided by Shanghai Jiao Tong University.

Declarations

Conflict of interest The authors declare no interest conflict. They have no known competing financial interests or personal relationships that could have appeared to influence the work reported in this paper.

Supplementary Information The online version contains supplementary material available at https://doi.org/10.1007/s40820-023-01221-3.

References

1. G. Wen, D.U. Lee, B. Ren, F.M. Hassan, G. Jiang et al., Orbital interactions in Bi-Sn bimetallic electrocatalysts for highly selective electrochemical CO_2 reduction toward formate production. Adv. Energy Mater. **8**, 1802427 (2018). https://doi.org/10.1002/aenm.201802427
2. C. Qiu, K. Qian, J. Yu, M. Sun, S. Cao et al., MOF-transformed In_2O_{3-x}@C nanocorn electrocatalyst for efficient CO_2 reduction to HCOOH. Nano-Micro Lett. **14**, 167 (2022). https://doi.org/10.1007/s40820-022-00913-6
3. J. Li, S.U. Abbas, H. Wang, Z. Zhang, W. Hu, Recent advances in interface engineering for electrocatalytic CO_2 reduction reaction. Nano-Micro Lett. **13**, 216 (2021). https://doi.org/10.1007/s40820-021-00738-9

4. S. Ji, Y. Qu, T. Wang, Y. Chen, G. Wang et al., Rare-earth single erbium atoms for enhanced photocatalytic CO_2 reduction. Angew. Chem. Int. Ed. **59**, 10651–10657 (2020). https://doi.org/10.1002/anie.202003623
5. K. Li, Y. Cai, X. Yang, S. Wang, C. Teng et al., H_2S involved photocatalytic system: a novel syngas production strategy by boosting the photoreduction of CO_2 while recovering hydrogen from the environmental toxicant. Adv. Funct. Mater. **32**, 2113002 (2022). https://doi.org/10.1002/adfm.202113002
6. R. Yang, Y. Fan, Y. Zhang, L. Mei, R. Zhu et al., 2D transition metal dichalcogenides for photocatalysis. Angew. Chem. Int. Ed. **62**, e202218016 (2023). https://doi.org/10.1002/anie.202218016
7. H. Guo, T. Yang, M. Yamamoto, L. Zhou, R. Ishikawa et al., Double resonance Raman modes in monolayer and few-layer $MoTe_2$. Phys. Rev. B **91**, 205415 (2015). https://doi.org/10.1103/PhysRevB.91.205415
8. K.A.N. Duerloo, Y. Li, E.J. Reed, Structural phase transitions in two-dimensional Mo- and W-dichalcogenide monolayers. Nat. Commun. **5**, 4214 (2014). https://doi.org/10.1038/ncomms5214
9. Y. Feng, C. Wang, P. Cui, C. Li, B. Zhang et al., Ultrahigh photocatalytic CO_2 reduction efficiency and selectivity manipulation by single-tungsten-atom oxide at the atomic step of TiO_2. Adv. Mater. **34**, 2109074 (2022). https://doi.org/10.1002/adma.202109074
10. G. Kresse, J. Furthmüller, Efficient iterative schemes for ab initio total-energy calculations using a plane-wave basis set. Phys. Rev. B **54**, 11169–11186 (1996). https://doi.org/10.1103/PhysRevB.54.11169
11. J.P. Perdew, K. Burke, M. Ernzerhof, Generalized gradient approximation made simple. Phys. Rev. Lett. **77**, 3865–3868 (1996). https://doi.org/10.1103/PhysRevLett.77.3865
12. G. Kresse, D. Joubert, From ultrasoft pseudopotentials to the projector augmented-wave method. Phys. Rev. B **59**, 1758–1775 (1999). https://doi.org/10.1103/PhysRevB.59.1758
13. V. Wang, N. Xu, J. Liu, G. Tang, W. Geng, Vaspkit: A user-friendly interface facilitating high-throughput computing and analysis using vasp code. Comput. Phys. Commun. **267**, 108033 (2021). https://doi.org/10.1016/j.cpc.2021.108033
14. S. Grimme, J. Antony, S. Ehrlich, H. Krieg, A consistent and accurate ab initio parametrization of density functional dispersion correction (Dft-D) for the 94 elements H-Pu. J. chem. phys. **132**, 154104 (2010). https://doi.org/10.1063/1.3382344
15. Z. Wang, J. Zhu, X. Zu, Y. Wu, S. Shang et al., Selective CO_2 photoreduction to CH_4 via $P^{d\delta+}$-assisted hydrodeoxygenation over CeO_2 nanosheets. Angew. Chem. Int. Ed. **61**, e202203249 (2022). https://doi.org/10.1002/anie.202203249
16. NIST-JANAF Thermochemical Tables. https://janaf.nist.gov/
17. Y.N. Bo, H.Y. Wang, Y.X. Lin, T. Yang, R. Ye et al., Altering hydrogenation pathways in photocatalytic nitrogen fixation by tuning local electronic structure of oxygen vacancy with dopant. Angew. Chem. Int. Ed. **60**, 16085 (2021). https://doi.org/10.1002/anie.202104001
18. Q. Li, C. Fang, Z. Yang, B. Yu, M. Takabatake et al., Modulating the oxidation state of titanium via dual anions substitution for efficient N_2 electroreduction. Small **18**, 2201343 (2022). https://doi.org/10.1002/smll.202201343
19. O.E. Dagdeviren, D. Glass, R. Sapienza, E. Cortés, S.A. Maier et al., The effect of photoinduced surface oxygen vacancies on the charge carrier dynamics in TiO_2 films. Nano Lett. **21**, 8348–8354 (2021). https://doi.org/10.1021/acs.nanolett.1c02853
20. A.S. Al-Fatesh, Y. Arafat, S.O. Kasim, A.A. Ibrahim, A.E. Abasaeed et al., In situ auto-gasification of coke deposits over a novel Ni-Ce/W-Zr catalyst by sequential generation of oxygen vacancies for remarkably stable syngas production via CO_2-reforming of methane. Appl. Catal. B Environ. **280**, 119445 (2021). https://doi.org/10.1016/j.apcatb.2020.119445
21. Y. Liu, Y. Zheng, W. Zhang, Z. Peng, H. Xie et al., Template-free preparation of non-metal (B, P, S) doped g-C_3N_4 tubes with enhanced photocatalytic H_2O_2 generation. J. Mater. Sci. Technol. **95**, 127–135 (2021). https://doi.org/10.1016/j.jmst.2021.03.025
22. X. Yao, X. Hu, W. Zhang, X. Gong, X. Wang et al., Mie resonance in hollow nanoshells of ternary TiO_2-Au-CdS and enhanced photocatalytic hydrogen evolution. Appl. Catal. B Environ. **276**, 119153 (2020). https://doi.org/10.1016/j.apcatb.2020.119153
23. H. Cheng, Q. Liu, Y. Diao, L. Wei, J. Chen et al., $CoMo_2S_4$ with superior conductivity for electrocatalytic hydrogen evolution: elucidating the key role of co. Adv. Funct. Mater. **9**, 2103732 (2021). https://doi.org/10.1002/adfm.202103732
24. S. Gong, Y. Niu, X. Liu, C. Xu, C. Chen et al., Selective CO_2 photoreduction to acetate at asymmetric ternary bridging sites. ACS Nano **17**, 4922–4932 (2023). https://doi.org/10.1021/acsnano.2c11977
25. C. Zhan, Y. Xu, L. Bu, H. Zhu, Y. Feng et al., Subnanometer high-entropy alloy nanowires enable remarkable hydrogen oxidation catalysis. Nat. Commun. **12**, 6261 (2021). https://doi.org/10.1038/s41467-021-26425-2
26. W. Liu, P. Fu, Y. Zhang, H. Xu, H. Wang et al., Efficient hydrogen production from wastewater remediation by piezoelectricity coupling advanced oxidation processes. PNAS **120**, e2218813120 (2023). https://doi.org/10.1073/pnas.2218813120
27. K.K. Halankar, B.P. Mandal, A.K. Tyagi, Superior electrochemical performance of MoS_2 decorated on functionalized carbon nanotubes as anode material for sodium ion battery. Carbon Trends **5**, 100103 (2021). https://doi.org/10.1016/j.cartre.2021.100103
28. X. Guo, E. Song, W. Zhao, S. Xu, W. Zhao et al., Charge self-regulation in 1T'''-MoS_2 structure with rich S vacancies for enhanced hydrogen evolution activity. Nat. Commun. **13**, 5954 (2022). https://doi.org/10.1038/s41467-022-33636-8
29. J.C. McGlynn, T. Dankwort, L. Kienle, N.A.G. Bandeira, J.P. Fraser et al., The rapid electrochemical activation of $MoTe_2$ for the hydrogen evolution reaction. Nat. Commun. **10**, 4916 (2019). https://doi.org/10.1038/s41467-019-12831-0

30. D. Lee, Y. Lee, Beneficial effect of V on stability of dispersed MoS_2 catalysts in slurry phase hydrocracking of vacuum residue: XAFS studies. J. Catal. **413**, 443–454 (2022). https://doi.org/10.1016/j.jcat.2022.06.037
31. J.Y. Zhang, J. Liang, B. Mei, K. Lan, L. Zu et al., Synthesis of Ni/NiO@MoO_{3-x} composite nanoarrays for high current density hydrogen evolution reaction. Adv. Energy Mater. **12**, 2200001 (2022). https://doi.org/10.1002/aenm.202200001
32. M. Krbal, V. Prokop, A.A. Kononov, J.R. Pereira, J. Mistrik et al., Amorphous-to-crystal transition in quasi-two-dimensional MoS_2: implications for 2D electronic devices. ACS Appl. Nano Mater. **4**, 8834–8844 (2021). https://doi.org/10.1021/acsanm.1c01504
33. X. Zhao, X. Li, Z. Zhu, W. Hu, H. Zhang et al., Single-atom Co embedded in BCN matrix to achieve 100% conversion of peroxymonosulfate into singlet oxygen. Appl. Catal. B Environ. **300**, 120759 (2022). https://doi.org/10.1016/j.apcatb.2021.120759
34. M. Cao, L. Ni, Z. Wang, J. Liu, Y. Tian et al., DFT investigation on direct Z-scheme photocatalyst for overall water splitting: $MoTe_2$/BAs van der Waals heterostructure. Appl. Surf. Sci. **551**, 149364 (2021). https://doi.org/10.1016/j.apsusc.2021.149364
35. M. Tan, Y. Ma, C. Yu, Q. Luan, J. Li et al., Boosting photocatalytic hydrogen production via interfacial engineering on 2D ultrathin Z-scheme $ZnIn_2S_4$/g-C_3N_4 heterojunction. Adv. Funct. Mater. **32**, 2111740 (2022). https://doi.org/10.1002/adfm.202111740
36. M. Humayun, N. Sun, F. Raziq, X. Zhang, R. Yan et al., Synthesis of ZnO/Bi-doped porous $LaFeO_3$ nanocomposites as highly efficient nano-photocatalysts dependent on the enhanced utilization of visible-light-excited electrons. Appl. Catal. B Environ. **231**, 23–33 (2018). https://doi.org/10.1016/j.apcatb.2018.02.060
37. Q. Zhang, S. Gao, Y. Guo, H. Wang, J. Wei et al., Designing covalent organic frameworks with Co–O_4 atomic sites for efficient CO_2 photoreduction. Nat. Commun. **14**, 1147 (2023). https://doi.org/10.1038/s41467-023-36779-4
38. L. Ran, Z. Li, B. Ran, J. Cao, Y. Zhao et al., Engineering single-atom active sites on covalent organic frameworks for boosting CO_2 photoreduction. J. Am. Chem. Soc. **144**, 17097–17109 (2022). https://doi.org/10.1021/jacs.2c06920
39. X. Chen, C. Peng, W. Dan, L. Yu, Y. Wu et al., Bromo- and iodo-bridged building units in metal-organic frameworks for enhanced carrier transport and CO_2 photoreduction by water vapor. Nat. Commun. **13**, 4592 (2022). https://doi.org/10.1038/s41467-022-32367-0
40. S. Yue, L. Chen, M. Zhang, Z. Liu, T. Chen et al., Electrostatic field enhanced photocatalytic CO_2 conversion on $BiVO_4$ nanowires. Nano-Micro Lett. **14**, 15 (2022). https://doi.org/10.1007/s40820-021-00749-6
41. Y. Zhang, Y. Li, X. Xin, Y. Wang, P. Guo et al., Internal quantum efficiency higher than 100% achieved by combining doping and quantum effects for photocatalytic overall water splitting. Nat. Energy **8**, 504–514 (2023). https://doi.org/10.1038/s41560-023-01242-7
42. J. Sheng, Y. He, J. Li, C. Yuan, H. Huang et al., Identification of halogen-associated active sites on bismuth-based perovskite quantum dots for efficient and selective CO_2-to-CO Photoreduction. ACS Nano **14**, 13103–13114 (2020). https://doi.org/10.1021/acsnano.0c04659
43. H. Li, C. Cheng, Z. Yang, J. Wei, Encapsulated CdSe/CdS nanorods in double-shelled porous nanocomposites for efficient photocatalytic CO_2 reduction. Nat. Commun. **13**, 6466 (2022). https://doi.org/10.1038/s41467-022-34263-z
44. J. Zhou, J. Li, L. Kan, L. Zhang, Q. Huang et al., Linking oxidative and reductive clusters to prepare crystalline porous catalysts for photocatalytic CO_2 reduction with H_2O. Nat. Commun. **13**, 4681 (2022). https://doi.org/10.1038/s41467-022-32449-z
45. C. Ban, Y. Duan, Y. Wang, J. Ma, K. Wang et al., Isotype heterojunction-boosted CO_2 photoreduction to CO. Nano-Micro Lett. **14**, 74 (2022). https://doi.org/10.1007/s40820-022-00821-9
46. L. Ju, X. Tan, X. Mao, Y. Gu, S. Smith et al., Controllable CO_2 electrocatalytic reduction via ferroelectric switching on single atom anchored In_2Se_3 monolayer. Nat. Commun. **12**, 5128 (2021). https://doi.org/10.1038/s41467-021-25426-5
47. Q. Cheng, M. Huang, L. Xiao, S. Mou, X. Zhao et al., Unraveling the influence of oxygen vacancy concentration on electrocatalytic CO_2 reduction to formate over indium oxide catalysts. ACS Catal. **13**, 4021–4029 (2023). https://doi.org/10.1021/acscatal.2c06228
48. D. Gao, J. Xu, L. Wang, B. Zhu, H. Yu et al., Optimizing atomic hydrogen desorption of sulfur-rich NiS_{1+x} cocatalyst for boosting photocatalytic H_2 evolution. Adv. Mater. **34**, 2108475 (2022). https://doi.org/10.1002/adma.202108475
49. C. Yang, B. Huang, S. Bai, Y. Feng, Q. Shao et al., A generalized surface chalcogenation strategy for boosting the electrochemical N_2 fixation of metal nanocrystals. Adv. Mater. **32**, 2001267 (2020). https://doi.org/10.1002/adma.202001267